Optical Materials 84 (2018) 475–489

Contents lists available at ScienceDirect

Optical Materials

journal homepage: www.elsevier.com/locate/optmat

Synthesis, crystal growth, structure and characterization of a novel third order nonlinear optical organic single crystal: 2-Amino 4,6-Dimethyl Pyrimidine 4-nitrophenol

P. Karuppasamy[a,*], T. Kamalesh[a], K. Anitha[b], S. Abdul Kalam[c], Muthu Senthil Pandian[a], P. Ramasamy[a], Sunil Verma[d,e], S. Venugopal Rao[c]

[a] SSN Research Centre, SSN College of Engineering, Chennai, 603110, Tamil Nadu, India
[b] Department of Physics, Madurai Kamaraj University, Madurai, 625021, Tamil Nadu, India
[c] Advanced Centre of Research in High Energy Materials (ACRHEM), University of Hyderabad, Gachibowli, Hyderabad, 500046, Telangana, India
[d] Laser Materials Section, Raja Ramanna Centre for Advanced Technology (RRCAT), Indore, 452013, Madhya Pradesh, India
[e] Homi Bhabha National Institute, Anushakti Nagar, Mumbai, 400094, Maharashtra, India

ARTICLE INFO

Keywords:
Crystal growth
X-ray diffraction
Hirshfeld
NMR
FTIR
Optical transmittance
TG-DTA
Hardness
LDT
Z-scan

ABSTRACT

Good quality single crystals of 2-amino-4,6-dimethylpyrimidine 4-nitrophenol (AMP4N) were successfully grown by slow evaporation solution technique (SEST) at room temperature using methanol as solvent. The grown crystal was subjected to single crystal XRD (SXRD) and its structure was solved by the direct method using SHELXS program and refined using SHELXL program. The Hirshfeld surfaces analysis was carried out to define theoretically electron density boundary surfaces between the molecules in a grown crystal, which are useful to analyze and view the intermolecular interactions. The powder XRD (PXRD) was carried out to identify the crystalline planes and its strain was also calculated by the Williamson–Hall equation. ^{13}C and ^{1}H NMR were recorded to interpret the environment of the molecular structure of the AMP4N crystal. Functional groups of AMP4N crystal were confirmed by Fourier transform infrared (FTIR) spectral analysis. The optical quality of the grown crystal was analyzed by UV–Vis NIR spectral analysis. The grown crystal has good optical transparency in the range 410–1100 nm. The thermal behaviour of the crystal has been investigated by thermogravimetric and differential thermal analysis (TG-DTA). Chemical etching study was carried out and the etch pit density (EPD) was calculated. The laser damage threshold (LDT) was measured under single-shot mode using an Nd: YAG laser at 532 nm. The third-order nonlinear optical properties such as refractive index (n_2), absorption coefficient (β) and susceptibility ($\chi^{(3)}$) were studied using the Z-scan technique at 532 nm with a continuous wave (CW) solid-state laser.

1. Introduction

In the last couple of decades there has been considerable research attention towards the synthesis of novel nonlinear optical (NLO) materials with superior properties because of their wide applications in the area of photonics, optoelectronics, optical information processing, THz wave generation, laser remote sensing, optical switching, pharmaceutical, color displays and frequency conversion, etc. [1,2]. The continuous research on organic NLO materials prompted researchers to explore many new NLO complexes engineered by the coupling of different organic molecules. When one uses chromophores with highly delocalized π electron systems, they lead to good macroscopic NLO response and high molecular hyperpolarizability. The pyrimidine and aminopyrimidine derivatives are biologically important compounds and they manifest themselves in nature as components of nucleic acids. The functions of nucleic acids are explicitly determined by hydrogen bonding patterns including base pairing which is responsible for genetic information transfer [3]. 4-nitrophenol is a phenolic organic compound of one-dimensional donor-π-acceptor (D-π-A) system which contains both electron accepting (NO_2) and electron-donating (OH) groups linked via aromatic benzene ring. The presence of OH groups favours the formation of new salts with various organic and inorganic bases [4]. 4-nitrophenol derivatives are promising NLO materials as they possess the linear D-π-A conjugated chains which give strong π-electron delocalization effect and these are prone to the formation of strong hydrogen bond interactions [5]. These interactions are known to play an

* Corresponding author. Tel.: +91 9791552297.
E-mail address: karuppasamyp75@gmail.com (P. Karuppasamy).

https://doi.org/10.1016/j.optmat.2018.07.039
Received 8 June 2018; Received in revised form 13 July 2018; Accepted 15 July 2018

important role in composing structures of co-crystals, structure of molecular crystals, biological systems, molecular recognition and crystal engineering research [6]. Hydrogen bonding is recognized as the most powerful force to organize molecules in the solid state and its employment is now emerging as an important design strategy [7]. In this case, the 2-amino-4,6-dimethylpyrimidine molecule is hydrogen bonded to the 4-nitrophenol molecule to form the novel co-crystalline material due to the strong interaction between pyrimidine and phenol. The main advantage of co-crystals is their ability to generate a variety of solid forms of a drug that have distinct physicochemical properties from the solid co-crystal components. These properties include but are not limited to, solubility, dissolution, bioavailability, hygroscopic nature, hydrate/solvate formation, crystal morphology, fusion properties, chemical and thermal stabilities, and mechanical properties [8]. Recently, π-conjugated organic systems have been extensively attracting candidates for synthesizing new efficient second and third order materials due to their quick NLO response. It must possess the enhanced figure of merit, large laser damage threshold (LDT) and low dielectric constant at higher frequencies [9].

In the present work, we have attempted to the synthesise new compound and grow optically transparent crystals of 2-amino-4,6-dimethylpyrimidine 4-nitrophenol (AMP4N) by slow evaporation solution technique (SEST). The grown crystals were characterized by single crystal X-ray diffraction (XRD), powder XRD, Nuclear magnetic resonance (NMR), Fourier transform infrared (FTIR), UV-Visible-NIR, thermogravimetric (TG) and differential thermal analysis (DTA), Vickers microhardness, chemical etching, Laser damage threshold (LDT) and third order nonlinear optical (NLO) studies (Z-scan).

2. Experiment

2.1. Material synthesis, crystal growth and morphology

Analytical reagent (AR) grade 2-amino-4,6-dimethylpyrimidine (AMP) and 4-nitrophenol (4NP) were taken in the stoichiometric ratio 1:1 for the synthesis of 2-amino-4,6-dimethylpyrimidine 4-nitrophenol co-crystalline compound. Initially, the calculated amount of AMP and 4NP were dissolved in methanol solvent. The solutions were mixed together using mechanical stirring for about 5 h. After that, it appeared as a light yellow colour solution. The prepared saturated solution was filtered twice into the crystallization dish by using Whatman filter paper and it was allowed to controlled evaporation at room temperature. After few weeks, the transparent yellow colour crystals were harvested. Then the purity of the synthesized material was further improved by successive recrystallization process to eliminate impurities. The optically transparent AMP4N single crystals have been grown over a period of 20 days. The reaction mechanism of the synthesized AMP4N crystal is depicted in Fig. 1. The photograph of as-grown AMP4N crystals is shown in Fig. 2. The morphology of the grown AMP4N crystal was indexed by a WinXMorph software program. The indexed morphology of AMP4N is shown in Fig. 3.

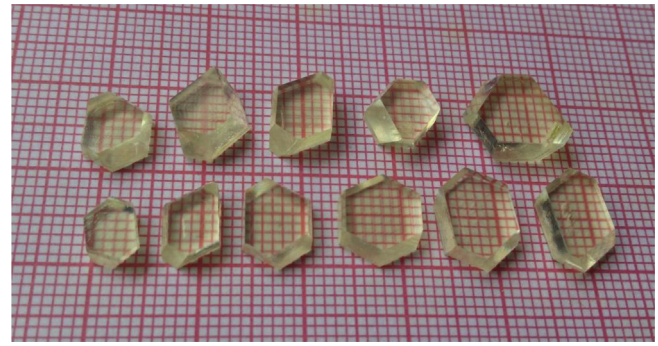

Fig. 2. As grown AMP4N single crystal.

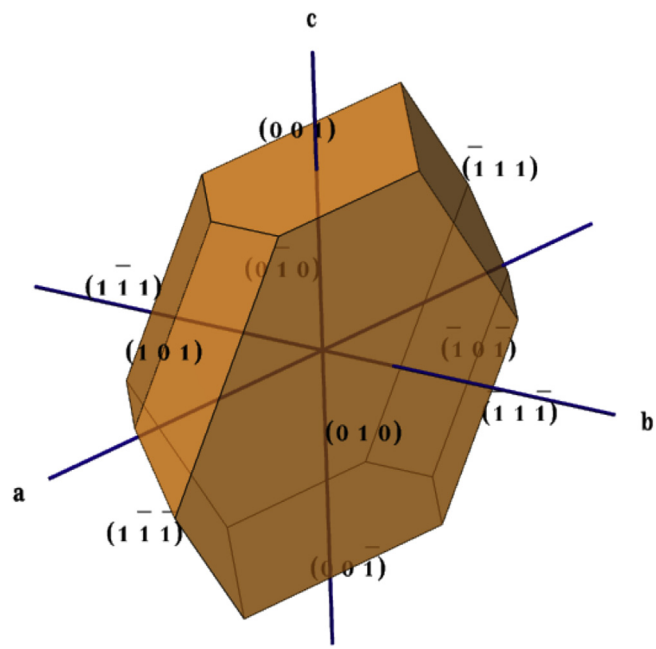

Fig. 3. Morphology of AMP4N single crystal.

2.2. Solubility

The solubility measurement is essential for the growth of bulk size single crystal. The solubility of the AMP4N crystal was determined for different temperatures ranging from 35 °C to 60 °C. This process has been carried out in a constant temperature bath (CTB) with the accuracy of ± 0.01 °C. Initially, the CTB was maintained at 35 °C. The solubility was determined by dissolving the recrystallized salts in 100 ml of methanol solvent in an airtight conical flask. The solution was continuously stirred by the help of immersible motorized magnetic stirrer.

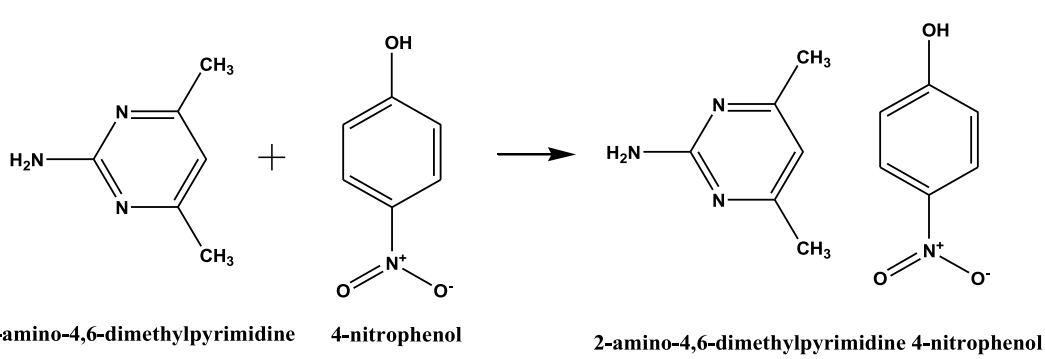

Fig. 1. Reaction scheme of AMP4N.

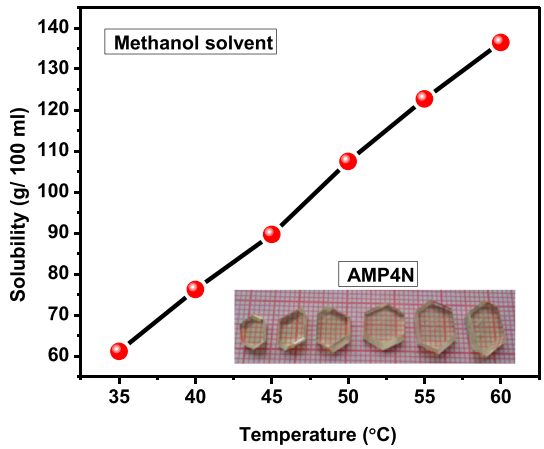

Fig. 4. Solubility curve of AMP4N as a function of temperature.

After attaining the saturation, the equilibrium concentration of the solution was analyzed gravimetrically. The same process was repeated to determine the solubility at different temperatures. The variation in solubility with temperature is shown in Fig. 4.

3. Characterization studies

The grown AMP4N crystal was subjected to the various characterizations. The Bruker kappa APEXII single crystal X-ray diffractometer with MoK_α (λ = 0.71073 Å) was used and the crystal structure was solved by using SHELXS direct method. The powder XRD was carried out using BRUKER X-ray diffractometer with the CuKα radiation (λ = 1.5406 Å). The NMR was carried out using Bruker AVANCE III 500 MHz (AV 500) multinuclei solution NMR Spectrometer. The FTIR spectrum of the AMP4N crystal was recorded in the range 400–4000 cm^{-1} using Bruker AXS FTIR spectrometer with KBr mode to analyze the various molecular vibrations of the compound at room temperature. The optical transmittance and the band gap of the grown crystal were studied using a Perkin-Elmer Lambda-35 UV–Vis NIR spectrophotometer in the region between 200 and 1100 nm. The thermal stability was identified by using Perkin-Elmer Diamond TG-DTA instrument. The as grown AMP4N crystals were subjected to Vickers microhardness measurement using the Shimadzu HMV-G20 microhardness tester fitted with the diamond indenter. The surface features of the crystal were identified using COSLAB Model CMM-23 optical microscope trinocular in the reflection mode. The Q-switched Nd: YAG laser of pulse width 7ns was used for laser damage threshold (LDT) analysis. The Z-scan technique was carried out on the grown crystal using a continuous wave (CW) solid-state laser (25 mW) of the wavelength of 532 nm.

4. Results and discussion

4.1. Single-crystal X-ray diffraction (SXRD)

The good quality AMP4N crystal was chosen for the X-ray diffraction measurement. The diffraction intensity data were collected using Enraf-Nonius CAD4 single crystal X-ray diffractometer with MoK_α (λ = 0.71073 Å) radiation at room temperature. The structure was solved by the direct method using the program SHELXS [10] which revealed the position of all the non-hydrogen atoms and refined on F^2 by a full matrix least squares method using SHELXL [10]. An anisotropic refinement of the non-hydrogen atoms was performed. All the hydrogen atoms were placed in geometrically calculated position and refined as a riding model with $U_{iso}(H)$ equal to 1.2 $U_{eq}(C)$ and 1.5U_{eq} (C, O) of the carrier atoms. The final structure converged to R_1 = 4.8% and wR_2 = 10.4%. The maximum and minimum peak heights in the final difference Fourier map were found to be 0.149 e. $Å^{-3}$ and -0.147e.$Å^{-3}$ respectively. Full crystallographic data (CIF file) relating to the crystal structure of AMP4N has been deposited with the Cambridge Crystallographic Database (CCDC 1565107). The molecular graphics were drawn using MERCURY software [11]. Details of the data collection, conditions and the refinement parameters are given in Table 1. The bond lengths and bond angles and torsion angles are given in the supplementary table (S. Table) 1 and 2 respectively.

Table 1
Crystallographic data for AMP4N crystal.

Identification code	AMP4N
Empirical formula	$C_{12}H_{14}N_4O_3$
Formula weight	262.27 g mol^{-1}
Temperature	293(2) K
Wavelength	0.71073 Å
Crystal system	Triclinic
Space group	P −1
Unit cell dimensions	a = 7.1947(4) Å b = 7.6830(5) Å c = 13.5411(5) Å α = 90.084(3)°, β = 97.541(5)°, γ = 116.791(3)°
Volume	660.83(6) $Å^3$
Z	2
Density (calculated)	1.318 Mg/m^3
Absorption coefficient	0.098 mm^{-1}
F(000)	276
Crystal size	0.150 × 0.150 × 0.100 mm^3
Theta range for data collection	2.977–25.000°.
Index ranges	−8 ≤ h < =8, −9 ≤ k < =9, −16 ≤ l < =15
Reflections collected	11553
Independent reflections	2288 [R (int) = 0.0560]
Completeness to theta = 25.000°	98.1%
Refinement method	Full-matrix least-squares on F^2
Data/restraints/parameters	2288/0/174
Goodness-of-fit on F2	1.023
Final R indices [I > 2sigma(I)]	R1 = 0.0477, wR2 = 0.1043
R indices (all data)	R1 = 0.1225, wR2 = 0.1343
Largest diff. peak and hole	0.149 and −0.147 e.Å-3

The present crystal structure belongs to triclinic system with space group P-1. The asymmetric unit of the present crystal structure contains 2-amino-4,6-dimethylpyrimidine and 4-nitrophenol molecules. Fig. 5 shows the ORTEP [12] view of the molecule drawn at 50% probability thermal displacement ellipsoids with the atom numbering scheme. Fig. 6 shows unit cell packing diagram of the present crystal structure. The formation of co-crystal is confirmed by N1-C6 (1.331(3) Å) bond length of pyrimidine ring and C11-O11 (1.346(3) Å) bond length of nitrophenol ring. The bond lengths N-C in the range 1.331(3) Å −1.348(3) Å are in good agreement with those observed in various carboxylic acid co-crystals with 2-amino 4,6-dimethylpyrimidine [13,14]. The molecular geometry of the 4-nitrophenol was comparable with the molecular complex of 2-amino-4-methylpyridinium 4-nitrophenolate-4-nitrophenol [15]. Both the pyrimidine and nitrophenol rings adopted planar configuration without any deviation from the plane and inclined nearly perpendicular to each other by an angle 86.14°. The structure is stabilized by strong N-H···O and O-H···N hydrogen bonds. The bond lengths and bond angles of hydrogen bond geometry are listed in Table 2. The inversion related pyrimidine molecules form a $R_2^2(8)$ ring motif through a pair of N3-H3B···N2 hydrogen bonds involving the 2-amino group (N3—H3B) and the pyrimidine N2 atom. The N3-H3A...O12 and N1-H1···O11 hydrogen bonds form a large ring motif with graph set notation $R_2^2(24)$. The two ring motifs are connected through nitrophenol and amino-pyrimidine moieties engaging in N3-H3B···N2, N3-H3A...O12 and N1-H1···O11 hydrogen bonds leading to the formation of the infinite linear ribbons and it is shown in Fig. 7.

4.1.1. Hirshfeld surface analysis

The Hirshfeld surfaces define the electron density boundary surfaces between the molecules in a crystal, which are useful to analyze and

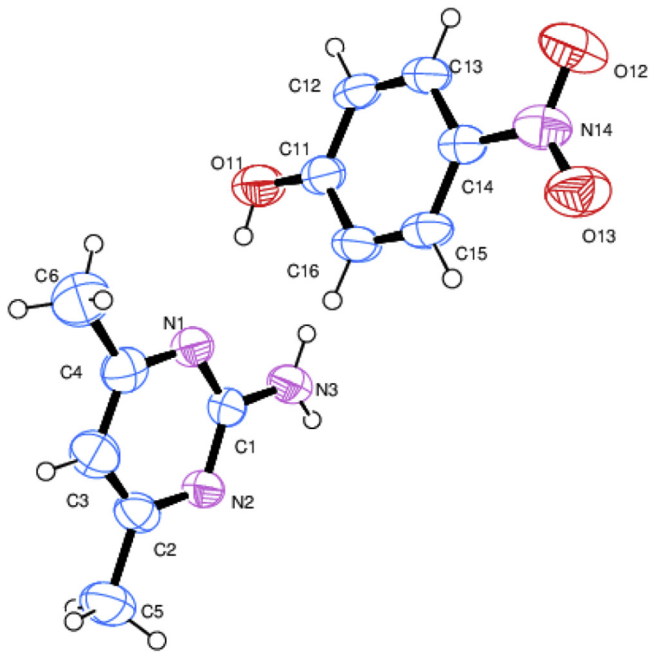

Fig. 5. Molecular diagram of AMP4N.

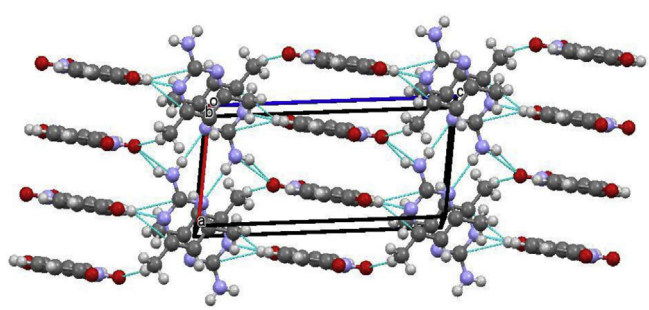

Fig. 6. Molecular packing diagram along b-axis.

Table 2
The hydrogen bond lengths (Å) and bond angles (°).

D-H...A	d(D-H) (Å)	d(H...A) (Å)	d(D...A) (Å)	< (DHA) (°)
O11-H11···N1	0.820	1.911	2.725	171.7
N3-H3A...O12(i)	0.860	2.234	3.009	149.8
N3-H3B···N2(ii)	0.860	2.213	3.070	175.8

(i) –x + 1, -y, -z + 1.
(ii) –x + 1, -y, -z.

view the intermolecular contacts. Calculations of Molecular Hirshfeld surfaces were performed using the Crystal Explorer program-3.1 [16,17]. Hirshfeld surfaces are mapped using the normalized contact distance (d_{norm}), which is calculated using the following equation.

$$d_{norm} = \frac{d_i - r_i^{vdw}}{r_i^{vdw}} + \frac{d_e - r_e^{vdw}}{r_e^{vdw}} \quad (1)$$

where d_e is the distance from the Hirshfeld surface to the nearest atom outside the surface, d_i is the distance from the Hirshfeld surface to the nearest atom inside the surface and d_{norm} is defined in terms of d_e and d_i and the van der Waals *(vdW)* radii of atoms. Three-dimensional (3D) Hirshfeld surface maps are generated with d_{norm}. While d_{norm} is negative where contacts shorter than *vdW* separations occur, and positive for contacts greater than *vdW* separations, and it is displayed using a red–white–blue colour scheme, where red highlights shorter contacts, white is used for contacts around the *vdW* separation, and blue is for longer

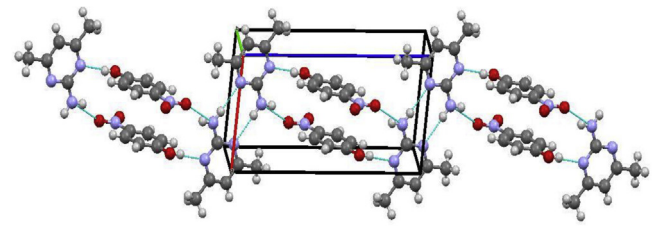

Fig. 7. Formation of the infinite linear ribbons of molecules.

contacts. Because d_{norm} is symmetric in d_e and d_i, any close intermolecular contact will be characterized by two identical red regions, although not necessarily on the same molecule. The 3D d_{norm} surfaces can be resolved into 2D fingerprint plots, analyzing the intermolecular contacts at the same time to quantitatively summarize the nature and type of all intermolecular contacts experienced by the molecules in the crystal. Hirshfeld surface and 2D fingerprint plots were generated from crystal data using CRYSTAL EXPLORER V.3.1. The red spots on the surfaces indicate the close-contact interactions, which are mainly responsible for the molecular packing in the crystals, which is shown in Fig. 8. The crystal packing is majorly controlled by dominant H- interactions involving ALL···ALL (100%); H···H (41.7%); C···O (1.7%); N···H (9.1%); O···H (26.7%) and C···H (10.1%) contacts, which are observed on the Hirshfeld surfaces analysis and picture representation of these interactions is shown in Fig. 9. From the data it is clear that H···H interaction dominates (with 41.7%) contributing highest percentage for the molecular packing stability.

4.2. Powder XRD

The powder X-Ray diffraction study for the crystal was carried out using BRUKER X-ray diffractometer with the CuKα radiation (λ = 1.5406 Å) with the step size of 0.050 s and scanning step time 10 s at room temperature in order to check the phase purity. The obtained XRD pattern for AMP4N is in good agreement with that of Rietveld refinement using the FullProf code (Fig. 10), which was performed on the *2θ* scans ranging from 10° to 80° and also the powder XRD spectrum obtained from CIF file. The obtained peaks have been indexed and the peaks are shown in Fig. 11. The well-defined refined peaks at specific *2θ* angles show a high degree of crystallinity of AMP4N. In the obtained diffraction pattern the high intensity and sharp peak indicate the high quality of the crystalline material, because the intensity of the diffracted beams from the different planes depends on the atomic arrangement in the crystal. Further, the strain present in the grown crystal was evaluated by using the Williamson–Hall equation [18]:

$$\beta \cos\theta = \frac{K\lambda}{\tau} + \eta \sin\theta \quad (2)$$

where *β, θ, K, λ, τ* and *η* are the FWHM of the diffraction peak, Bragg diffraction angle of the peak in radian, Scherrer constant, wavelength of X-rays, crystallite size and strain, respectively. The value of the strain was calculated by plotting *βcosθ* versus *sinθ* as shown in Fig. 12. These data were fitted linearly to obtain the strain value from the slope of the fitted line. The slope value *(η)* is 0.4696 with an error of ± 0.1405. The minimum value of *η* indicated that the grown crystal has less lattice strain.

4.3. NMR analysis

The ^{13}C NMR and ^{1}H NMR spectral analyses are used to study the carbon and hydrogen skeleton of the AMP4N single crystal. NMR spectra were recorded in DMSO solvent using BRUKER Avance 400 MHz FT-NMR spectrometer. The ^{13}C NMR spectrum of the AMP4N crystal is shown in Fig. 13. The signals at the chemical shift value of δ35.90 ppm is attributed to the two carbons (C5 and C6) in the form of –CH_3 groups of the 2-amino-4,6-dimethylpyrimidine moiety. These two methyl groups are bonded to the fourth (C2) and sixth place (C4) of

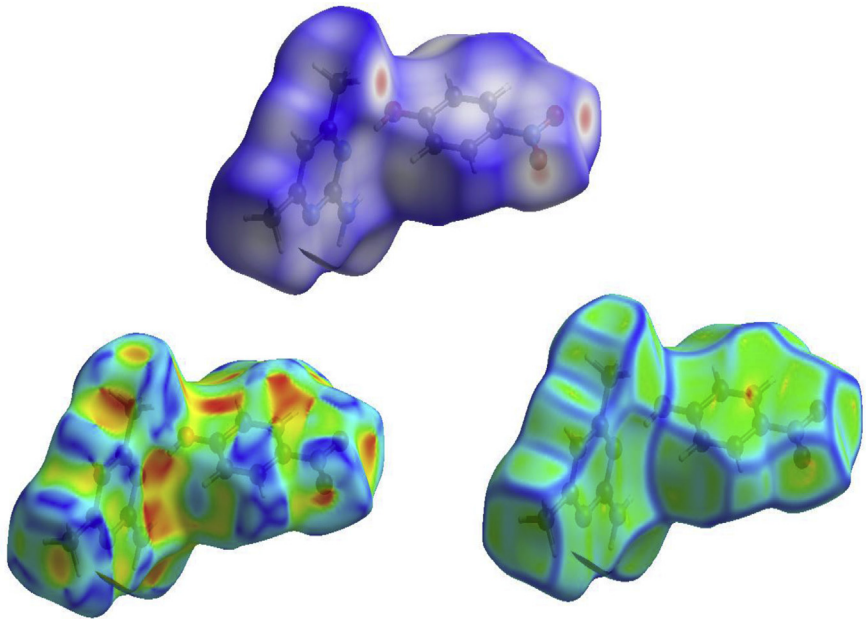

Fig. 8. Hirshfeld surfaces mapping of AMP4N molecule.

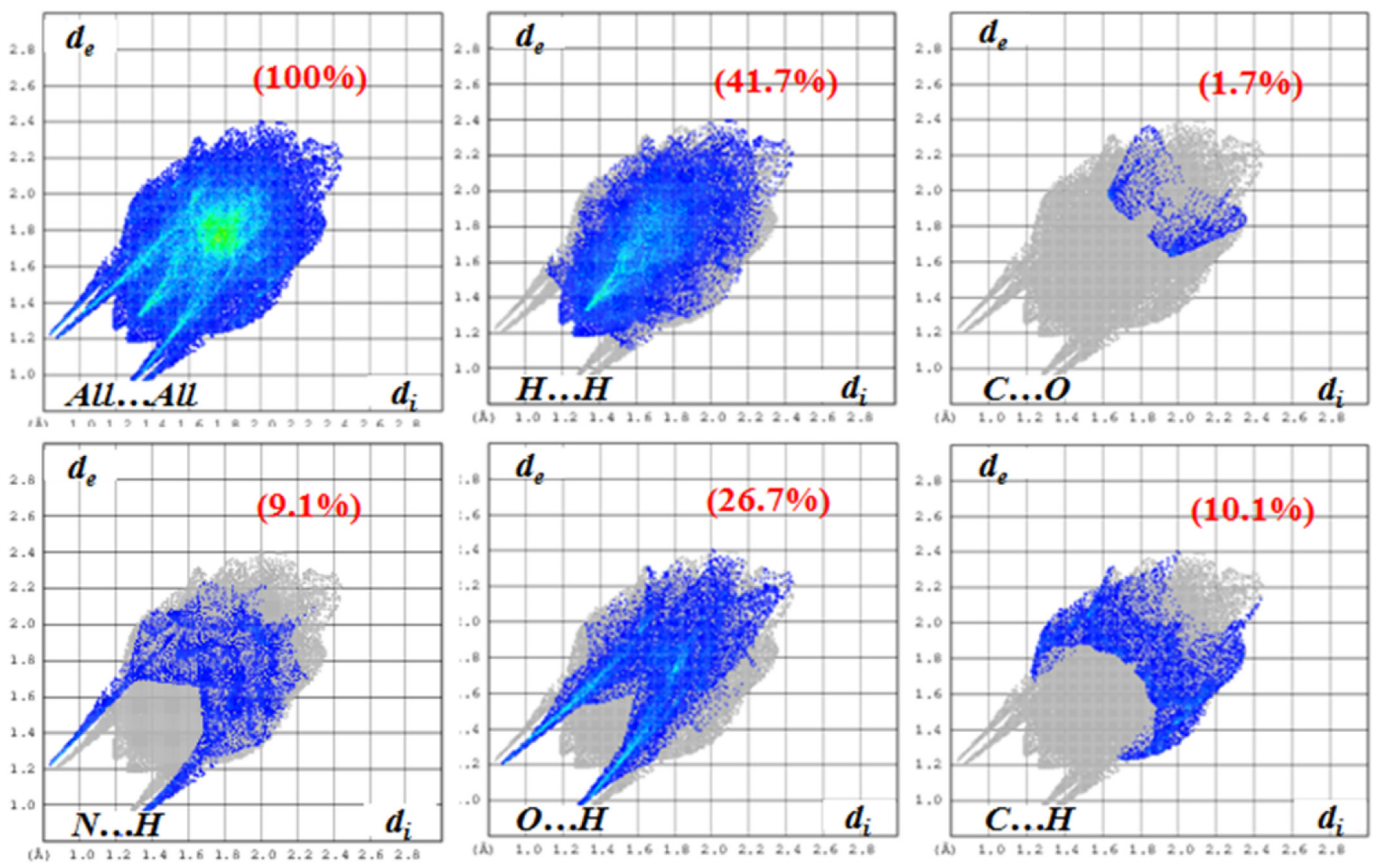

Fig. 9. The mapping of hydrogen bond interactions.

carbons present in a benzene ring and their chemical shift value was found to be δ167.24 ppm. The shift at δ163.75 ppm indicates that the carbon (C1) is placed in a benzene ring with the amine (-NH_2) group. The shift at δ 109.11 ppm indicates the remaining carbon (C3) of the same benzene ring. The nitrophenol molecule contains six carbon atoms. The chemical shift values δ 116.20 ppm and δ126.57 ppm represent C12, C16 and C13, C15 respectively. The nitro (-NO_2) group attached carbon (C14) is represented by the δ140.02 ppm and the hydroxyl (OH) group attached carbon (C11) is represented by chemical shift at δ 164.40 ppm. The ^{1}H NMR spectrum of the AMP4N crystal is shown in Fig. 14. The peak with chemical shift value at δ 2.157 ppm is assigned to two methylene protons of the 2-amino-4,6-dimethylpyrimidine moiety. The chemical shift at δ 6.321 ppm is due to the influence of –CH protons in a AMP. The shift at δ 6.375 ppm is attributed to

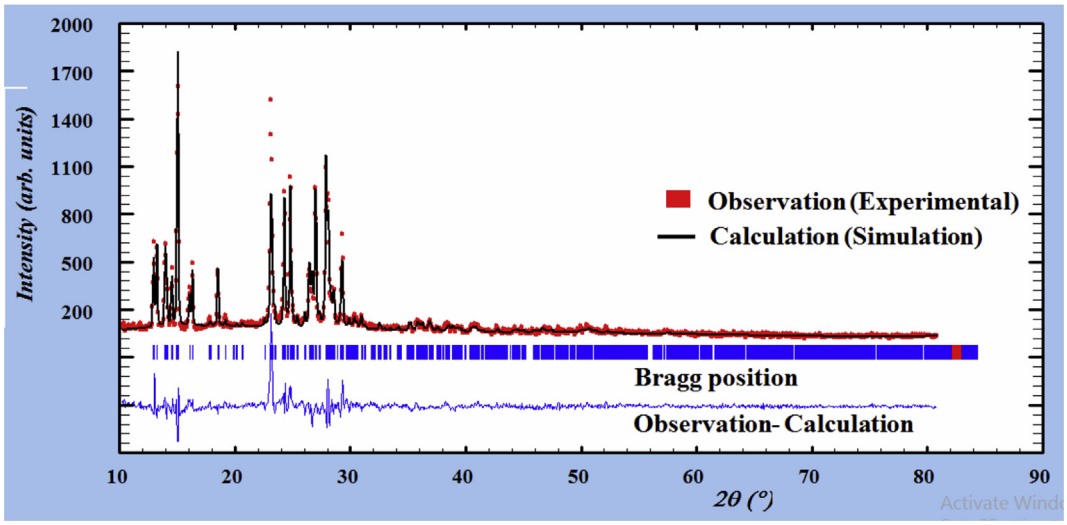

Fig. 10. Rietveld refinement using the FullProf code.

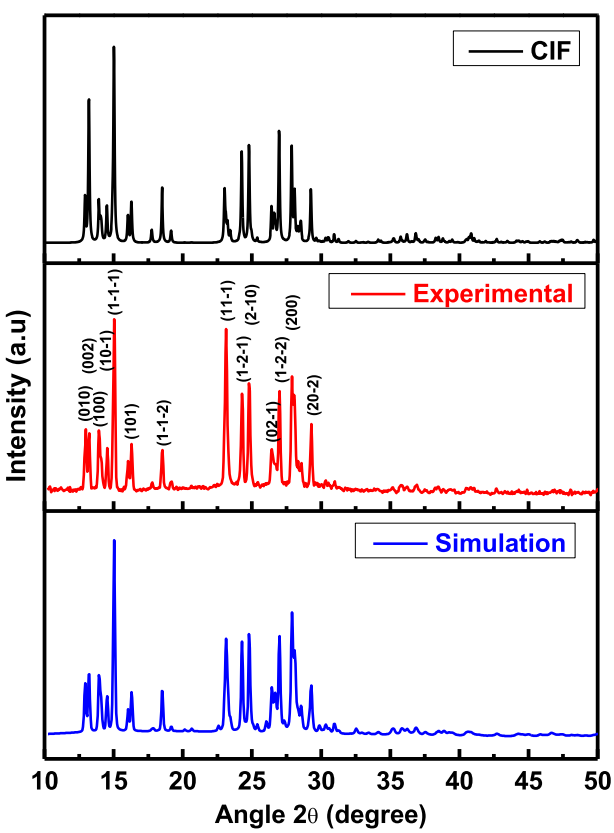

Fig. 11. Powder XRD pattern of AMP4N.

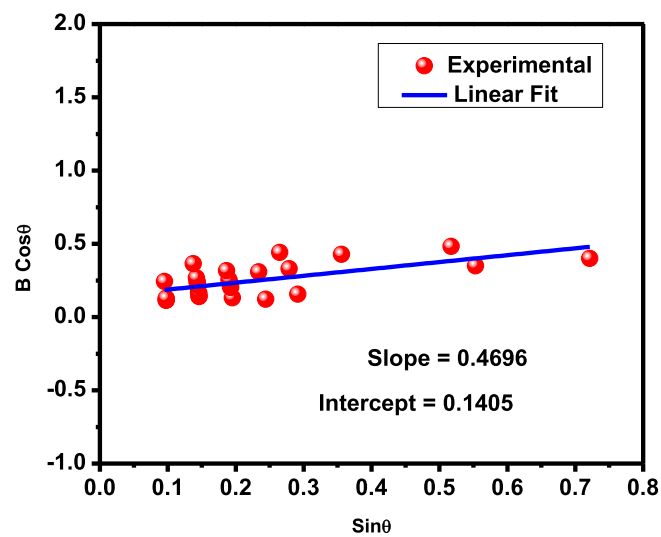

Fig. 12. Graph plotting $\beta cos\theta$ versus $sin\theta$.

the protons present in amine (-NH_2) group. The presence of the signal at δ 6.906–6.960 ppm and δ 8.095–8.148 ppm indicates the protons (e and f) presence in a benzene ring and δ 11.061 ppm is due to the proton in a phenol (OH) group of nitrophenol molecule. The peaks δ 2.500–5.511 ppm and δ 3.365 ppm are verified and these are due to the impurities present in a solvent. The NMR spectra analysis confirms the AMP4N carbon hydrogen framework.

4.4. FTIR analysis

Fourier transform infrared (FTIR) spectroscopy is an analytical technique used to identify the functional groups of the grown AMP4N crystal. FTIR analysis provides information about the chemical bonding and molecular vibration of a material. The FTIR spectrum of the grown crystal was analyzed using KBr pellet technique at room temperature in the wavenumber range between 400 cm^{-1} to 4000 cm^{-1}. The FTIR spectrum of AMP4N is shown in Fig. 15. The FTIR spectrum of AMP crystal was reported [19]. The peak observed at 3343 cm^{-1} is assigned to OH strong stretching vibration [20]. The peak at 3324 cm^{-1} indicates NH_2 symmetric stretching vibrations. The peak at 3169 cm^{-1} indicates the absorption of N-H stretching mode. The peak at 1650 cm^{-1} is assigned to the strong C=O stretching. The peak 1584 cm^{-1} represents the asymmetric NO_2 stretching [21–23]. The peak at 1497 cm^{-1} belongs to antisymmetric NO_2 stretching [24]. The peak at 1384 cm^{-1} denotes NO_2 symmetric stretching. The observed peak at 1333 cm^{-1} represents the NO_2 symmetric vibration [21,22]. The O–H in-plane bending (C–NO_2) stretch mode occurred at 1170 cm^{-1}. The N–H ….O in-plane bending is observed at 1105 cm^{-1}. The peak at 840 cm^{-1} is due to C–C–C deformation of phenol ring vibration. The vibration band at 750 cm^{-1} is attributed to CH_2 rocking vibration. The peak at 632 cm^{-1} is assigned to C–C–O deformation (phenol ring) [25].

4.5. UV–Vis NIR spectral analysis

The optically good quality single crystals are mainly useful for optical device applications. The transmittance properties are closely

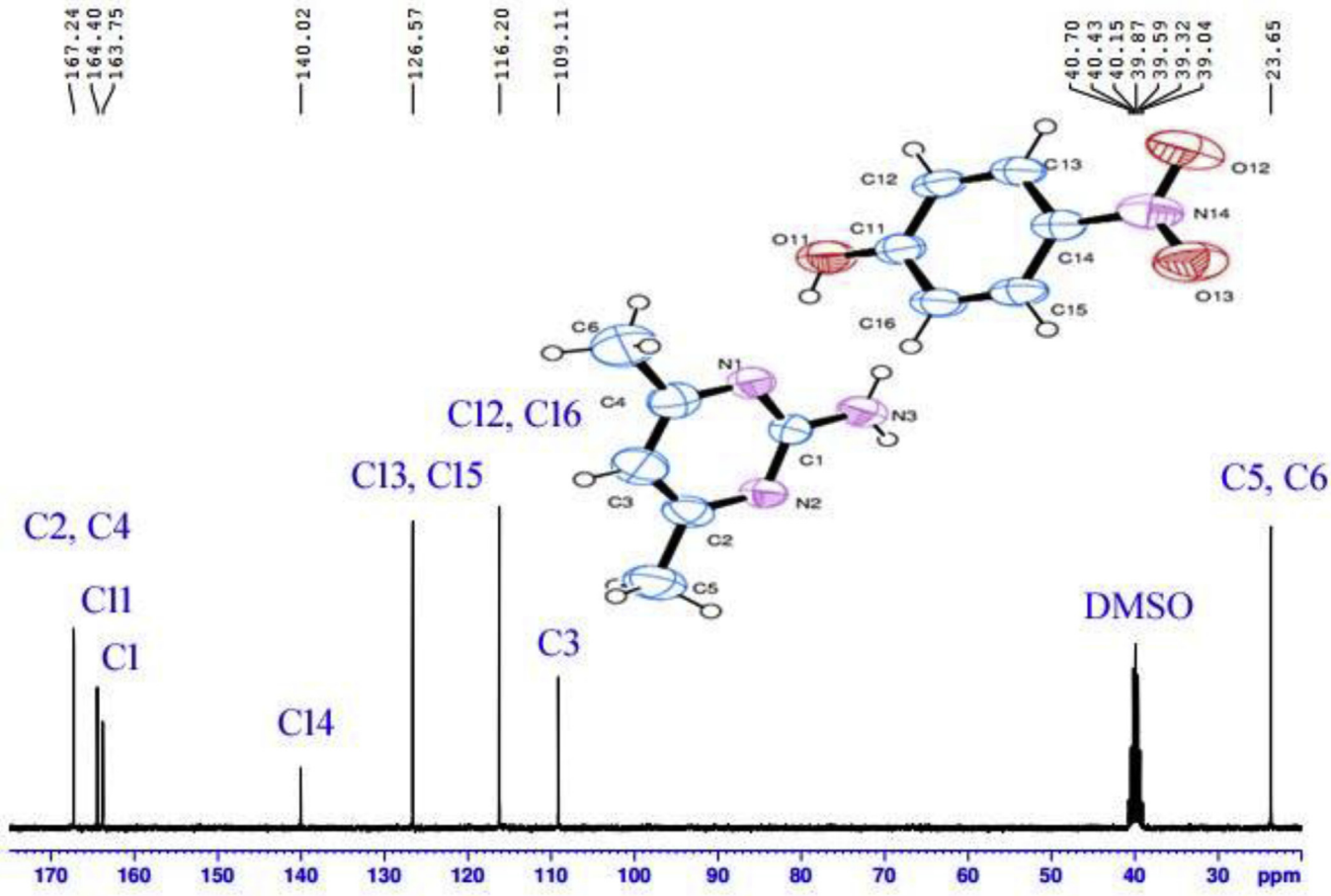

Fig. 13. ^{13}C NMR spectrum of AMP4N.

related to the atomic structure, electronic bandgap and also the physical quality of the material. The optical transmittance spectrum of the AMP4N single crystal was recorded and the data is illustrated in Fig. 16. From the UV–Vis NIR spectrum, it was observed that the grown crystal shows good optical transmittance at entire visible and near IR region with lower cut off at 405 nm. The NLO property of the organic material is determined by a complex contribution of the intra- and inter-molecular hyperpolarizabilities [26,27]. When the electromagnetic radiation interacts with materials, it will get absorbed at the certain range of wavelength due to charge transfer. The present system consists of strong N-H…O intermolecular hydrogen bonding, which is caused by charge transfer. The two ring motifs nitrophenol and amino-pyrimidine molecules are connected and engaging in N3-H3B···N2, N3-H3A...O12 and N1-H1···O11 hydrogen bonds. These chains are leading to the formation of three dimensional (3D) network. Normally the dipolar molecules possessing an electron donor and an electron acceptor group contribute to enhancing optical nonlinearity arising from the intramolecular charge transfer. The absorption edge at 405 nm may be assigned to n→ π* state. The optical absorption coefficient *(α)* dependence on the photon energy *(hυ)* helps to study the band structure and the type of transition of electrons. The optical transmittance data have been used to evaluate various optical parameters. The dependence of the optical absorption coefficient with the photon energy helps to study the band structure and the type of transition of electrons. According to the Tauc's plot relation, the optical band gap of the AMP4N single crystal was calculated [28].

$$(\alpha h\upsilon) = A(h\upsilon - E_g)^m \tag{3}$$

where α is the absorption coefficient, $h\upsilon$ is photon energy, E_g is the optical energy band gap, A is a constant and m is the characteristics of transitions. Normally the probability of electron transition between the valence band and conduction band can be either direct or indirect and also both have forbidden transitions [29]. The transition number *(m)* gives the details about the type of optical transitions. In general, it is noticed that, 1/2 is for direct allowed transition, 2 for indirect allowed transition, 3/2 for direct forbidden transition and 3 for the indirect forbidden transition. In this case, we have to determine the value of 'm' and it indicates the optical transition nature of the grown single crystal. Taking logarithm on both sides and differentiating the equation (3) with respect to $h\upsilon$ we get the following form [30].

$$\ln(\alpha h\upsilon) = \ln(A) + m\ln(h\upsilon - E_g) \tag{4}$$

$$\frac{d(\ln(\alpha h\upsilon))}{d(h\upsilon)} = \frac{m}{(h\upsilon - E_g)} \tag{5}$$

The value of E_g can be calculated from a graph plotted between *(ln (αhυ))/hυ* and *hυ* which is shown in Fig. 17 (a). From this figure, there is a single stage of optical transition with a discontinuity at maximum energy value of knee point (E_g = 3.05 eV). Plotting the graph between *(ln (αhυ))* and *(ln (hυ-E_g))* the value of *m* is obtained. The value of *m* was found to be 0.41 ≈ 0.5 ≈ 1/2 by extrapolating linear fit as shown in Fig. 17 (b). This confirms that the optical transition of the AMP4N crystal is allowed direct band gap in nature. Hence the Tauc's plot relation has been rearranged for direct allowed transition as given below [28]:

$$(\alpha h\upsilon) = A(h\upsilon - E_g)^{\frac{1}{2}} \tag{6}$$

A graph is plotted between photon energy *(hυ)* and *(αhυ)*^{2}. By extrapolating the linear portion of the curve to zero absorption as shown

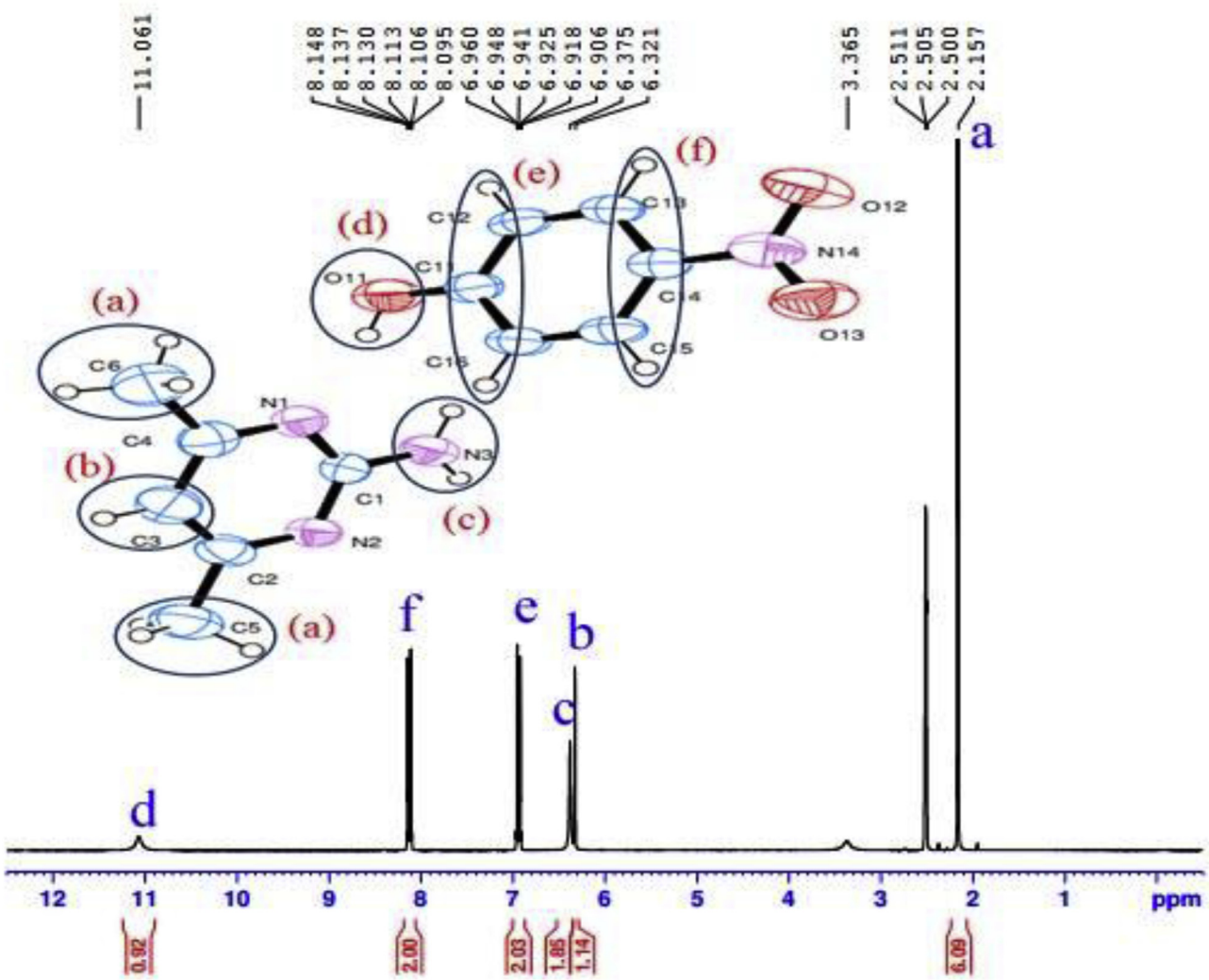

Fig. 14. ^{1}H NMR spectrum of AMP4N.

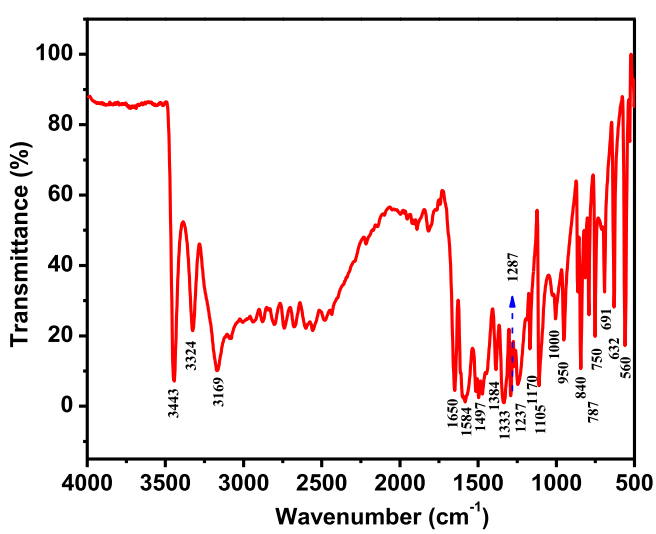

Fig. 15. FTIR spectrum of AMP4N single crystal.

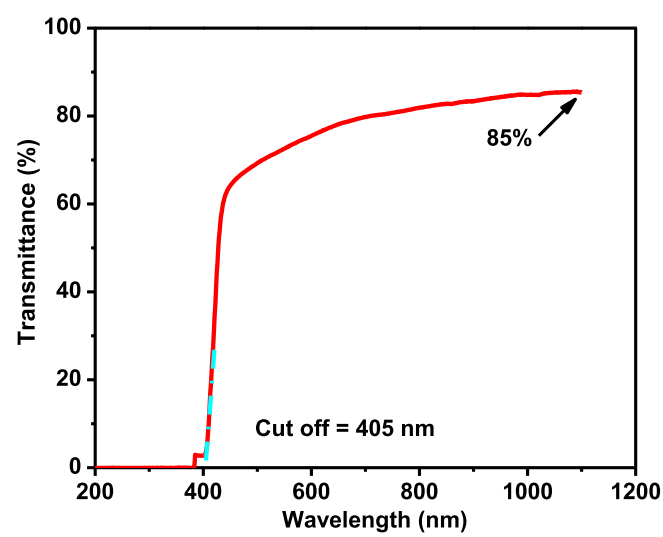

Fig. 16. UV–Vis NIR spectrum of AMP4N single crystal.

in Fig. 17 (c)

$$\alpha = \frac{2.3026}{t}\log_{10}\left(\frac{100}{T}\right) \tag{7}$$

where T is the transmittance (%) and t is the thickness of the sample (1 mm). The calculated direct band gap energy of AMP4N single crystal was 3 eV. Theoretical optical band gap energy of AMP4N crystal was calculated using the formula:

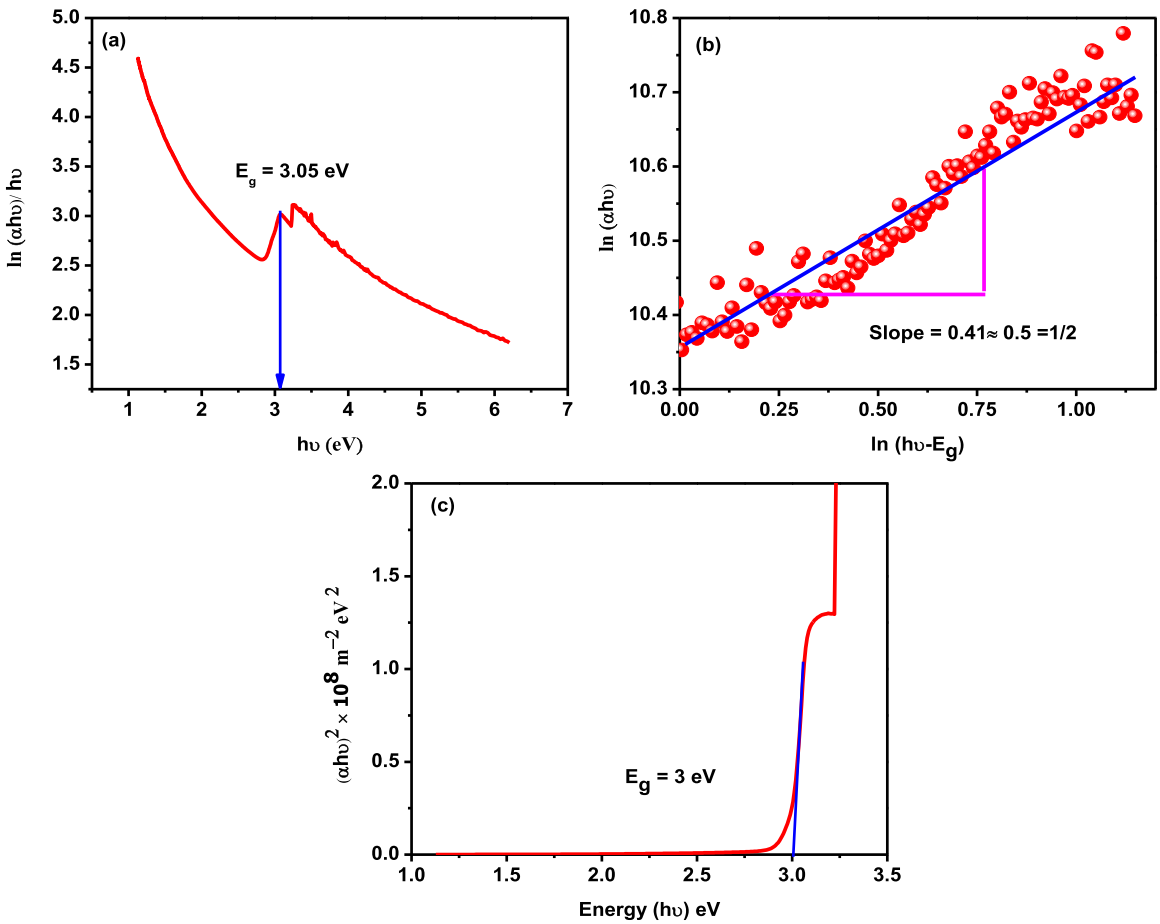

Fig. 17. (a) Plot of *(ln (αhυ))/hυ* versus *hυ*, (b) Plot of *(ln (αhυ))* versus *(ln (hυ - E_g))* and (c) Optical Band gap spectrum.

$$E_g = \frac{1240}{\lambda} eV \tag{8}$$

where λ is the lower cut-off wavelength (405 nm). The band gap of the grown AMP4N crystal is found to be 3.06 eV, which is in good agreement with the value obtained from Fig. 17 (a) and Fig. 17 (c).

The extinction coefficient *(K)* explains the amount of absorption of the electromagnetic wave propagating through a material and it is calculated using the following relation:

$$K = \frac{\alpha\lambda}{4\pi} \tag{9}$$

where *α* is the absorption coefficient and λ is the wavelength of light. The variation of extinction coefficient *(K)* with wavelength is shown in Fig. 18 (a). The reflectance *(R)* and refractive index *(n_o)* in terms of the absorption coefficient *(α)* can be derived from the following relation.

$$R = \frac{\exp(-\alpha t) \pm \sqrt{\exp(-\alpha t)T - \exp(-3\alpha t)T + \exp(-2\alpha t)T^2}}{\exp(-\alpha t) + \exp(-2\alpha t)T} \tag{10}$$

It is observed that the reflectance *(R)* increases with an increase in the photon energy and it is shown in Fig. 18 (b). The transmission *(T)* and reflectance *(R)* spectra can be used to calculate the refractive index *(n_0)* of AMP4N crystal from the following equation.

$$n_0 = -(R+1) \pm 2\frac{\sqrt{R}}{(R-1)} \tag{11}$$

The linear refractive index *(n_0)* of AMP4N crystal was determined in terms of reflectance *(R)* using the relation (11). The linear refractive index *(n_0)* of the grown crystal was found to be 2.26 at the wavelength of 532 nm. Fig. 18 (c) shows the variation of refractive index *(n_0)* as a function of wavelength and it is used to calculate the third order non-linear optical susceptibility *($\chi^{(3)}$)* of AMP4N crystal.

4.6. Thermal studies

The thermal stability of the grown AMP4N single crystal was studied using TG-DTA. 1.5 mg of crystalline sample was taken in an alumina crucible. Nitrogen gas was allowed to pass inside the furnace to maintain a constant inert atmosphere. The sample was heated in the range of 30 °C–250 °C with the heating rate of 10 °C/min. The TG and DTA graph is shown in Fig. 19. The AMP4N crystal exhibits a single stage decomposition and it starts from around 120 °C–210 °C with a mass loss of 100% of the material. It is due to the liberation of volatile reaction products such as NO_2, NO, CO_2 and CH [31]. In the present case, there is no weight loss observed between 30 °C and 120 °C. It shows that the crystal was thermally stable upto 120 °C. The DTA curve shows single endothermic peak which illustrates the decomposition of the AMP4N compound between 120 °C and 210 °C.

4.7. Microhardness studies

The mechanical strength of the material has a key role in the practical device fabrication. Transparent AMP4N single crystals, free from cracks with flat and smooth faces are chosen for static indentation Vickers microhardness test. The crystal was mounted on the base of the

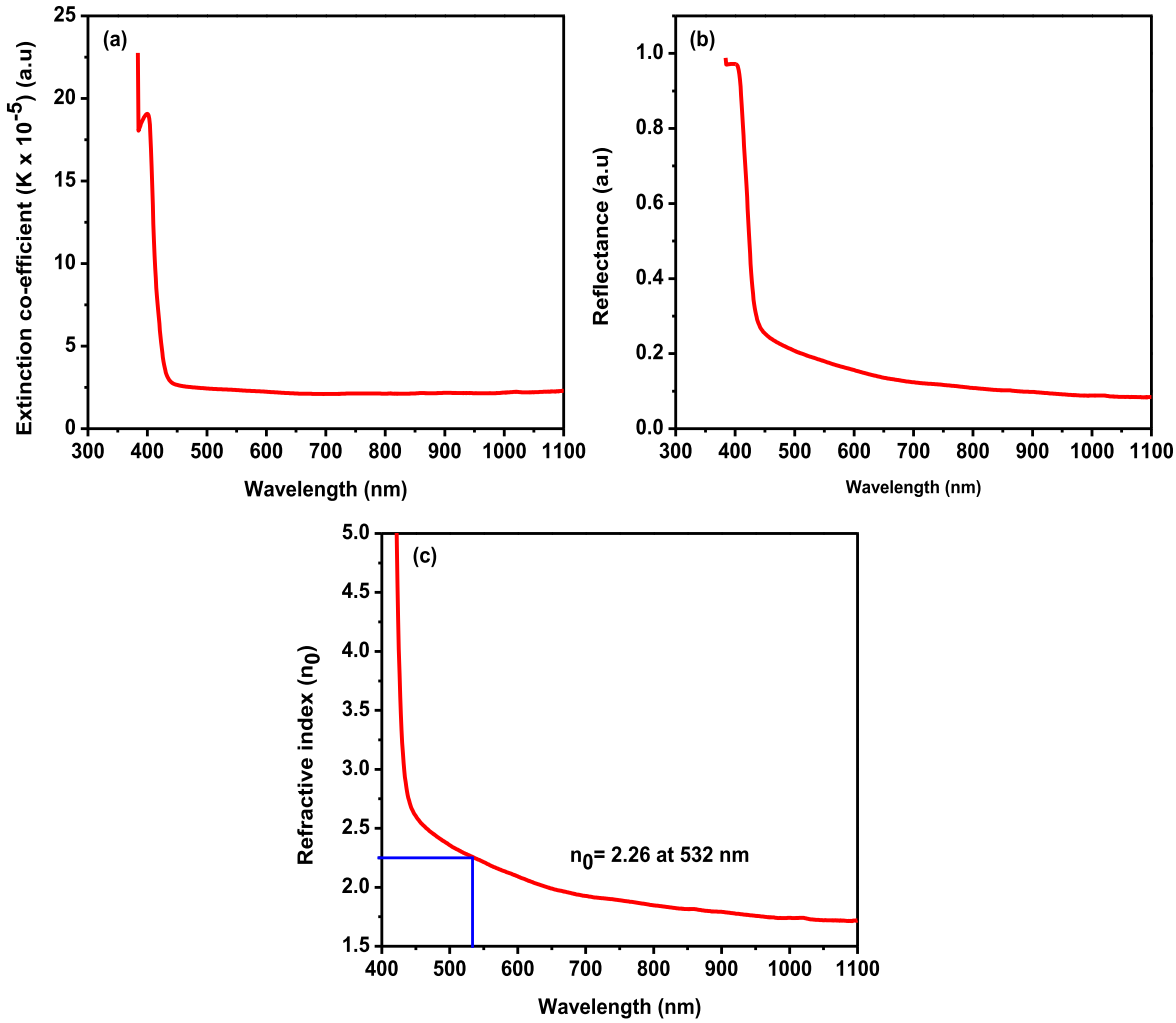

Fig. 18. Wavelength dependence of (a) Extinction co-efficient *(K)*, (b) Reflectance *(R)* and (c) Refractive indices *(n_0)*.

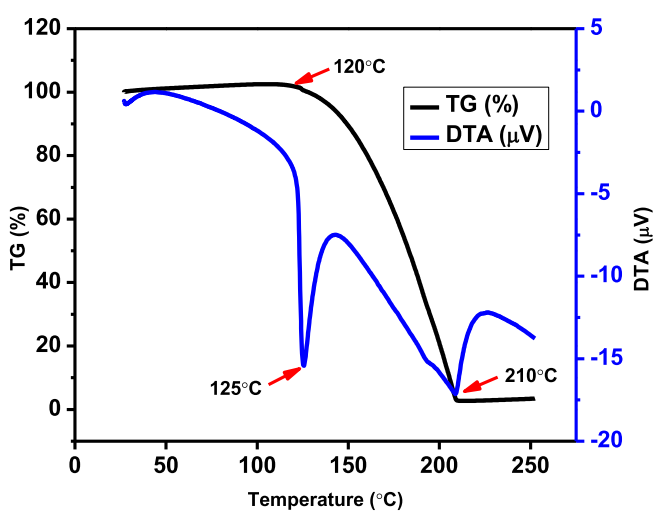

Fig. 19. TG-DTA analysis of AMP4N single crystal.

microscope and loads starting from 10 g to 100 g were given to the top surface of the AMP4N crystal plane (010) at different places using 136° triangular pyramid indenter. The static indentations were made with a constant indentation time of 5 s for all the loads. For each load, the diagonal length *(d)* was observed and the average of these values was considered. The Vickers hardness number *(H_v)* is calculated using the following relation [32].

$$H_v = 1.854\frac{P}{d^2}kg/mm^2 \tag{12}$$

where P is the applied load *(kg)* and d is the diagonal length (mm). A plot obtained between the hardness number *(H_v)* and the applied load *(P)* is depicted in Fig. 20. It shows that the hardness number increases with the increase of applied load upto 100 g. This indicates that the crystal exhibits reverse indentation size effect *(RISE)* [33]. The indentation impressions obtained for different loads on AMP4N crystal are shown in Fig. 21. The value of work hardening coefficient *(n)* can be calculated using Meyer's relation [34].

$$P = Ad^n \tag{13}$$

where A is constant for a given material and n the work hardening coefficient of the AMP4N single crystal. $n < 2$ is the normal ISE behaviour. When $n > 2$, there is the reverse ISE behaviour. When $n = 2$, the hardness is independent of applied load and it is given by Kick's law. The value of n can be calculated from Meyer's graph of *log P* versus *log d* and fitting data by least squares gives straight line as shown in Fig. 22. The value of n was found to be 3.4.

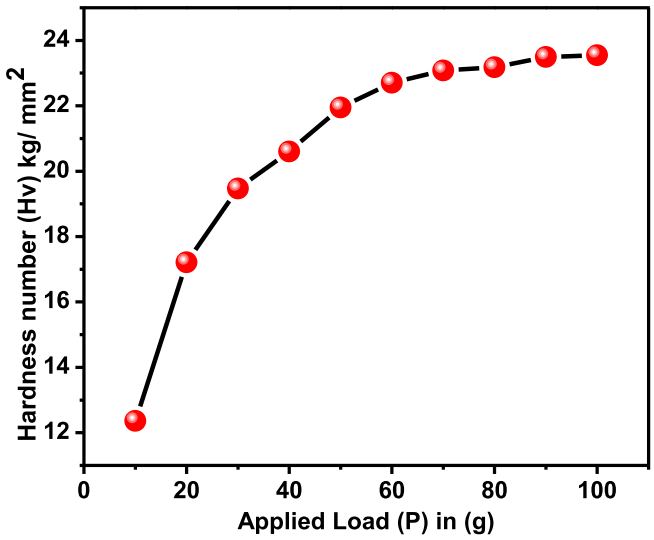

Fig. 20. Variation of H_v versus *load P*.

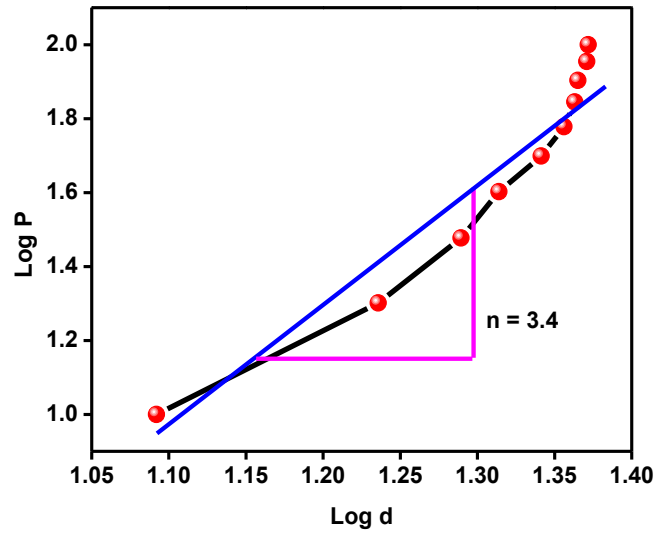

Fig. 22. Graph plotting '*log P*' versus '*log d*'.

4.8. Chemical etching analysis

The chemical etching was carried out for as grown AMP4N single crystal on (010) plane to determine the distribution of dislocations. Good quality with transparent AMP4N single crystal was selected and it is soaked with mixed solvent (water + methanol) as an etchant. For every soak, the surface features of the grown crystal were identified by an optical microscope. The etch pit patterns were obtained for various times such as 2 s, 4 s and 6 s. The obtained etch pits are shown in Fig. 23. Well defined triangular shaped etch pits have been obtained. The etch pits were randomly distributed but strictly oriented. When the etching time increased the pit size also enlarged and finally the etch pits overlapped. The etch pit density *(EPD)* of the grown crystal was found to be 1.4×10^3 cm^{-2}.

4.9. Laser damage threshold (LDT)

Nonlinear crystals with a high damage threshold, wide angle of phase matching, high transparency and large effective nonlinear coefficients are attractive materials for high-power frequency converters. In particular, for power laser applications, the laser-induced damage threshold determines their limit of performance. The damage threshold depends not only on the intrinsic material parameters (linear absorption, self-focusing, multiphoton absorption, stimulated Brillouin scattering, stimulated Raman scattering, and electron avalanche breakdown) but also on the laser beam parameters (pulse duration, beam spot size, transverse and longitudinal laser modes, and laser wavelength) [35]. The surface damage requires a laser that has a controlled TEM_{00} mode with outputs of only a few mJ making it necessary to focus sharply in order to obtain energy densities high enough to cause damage. In the present case, Nd:YAG laser (532 nm, pulse width 7 ns) was used to determine the laser damage threshold value of AMP4N crystal. A laser beam of 8 mm diameter and the convex lens of focal length *(f)* 10 cm were used to focus on the sample table (made up of copper plate). The schematic diagram of LDT measurement is shown in Fig. 24. The good quality crystal of thickness 5 mm was used and the surface of the samples was fixed at 5 mm above from the actual focal point of the convex lens. The laser beam was focused on the crystal (010) plane and every single shot was initiated at different places of same plane and its power has been varied such as 5, 10, 15, 20, 30, 40, 60, 70 and 80 mJ. No damage spot was observed in the crystal while power varied from 5 to 10 mJ but a small dot appeared from 15 mJ. The dot size increased when increasing input energy up to 30 mJ, further increasing the energy the constant damage size was observed. The circular heat dissipation started to appear around the damage spot at 70 mJ. The crystal has orderly damage spot, heat distribution around the spot and bulk damage was observed. The damage patterns of the AMP4N crystal are shown in Fig. 25. The surface damage threshold of the grown AMP4N crystal was calculated using the expression.

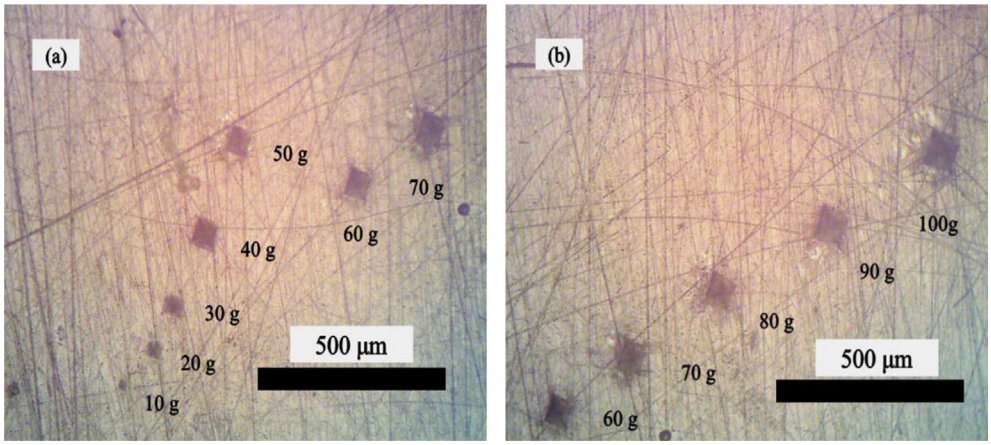

Fig. 21. Indentation of AMP4N crystal.

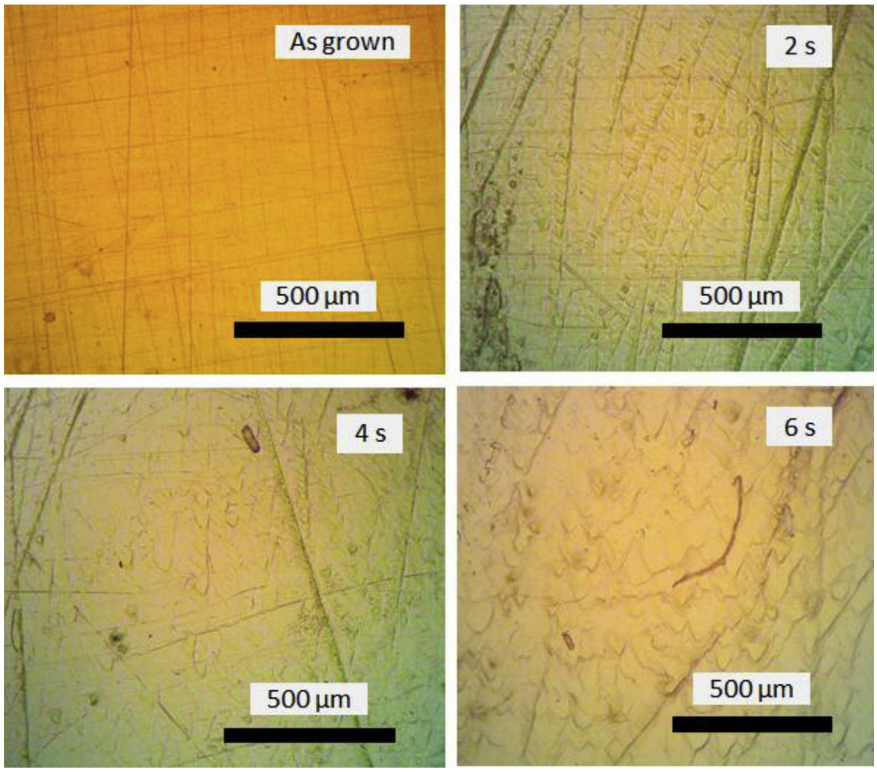

Fig. 23. Chemical Etch pits of AMP4N single crystal on (010) plane, (a) as grown crystal, (b) 2 s (c) 4 s and (d) 6 s etched surface.

$$\text{Power density}(P_d) = \frac{E}{\tau\pi(\omega_Z)^2} \tag{14}$$

where, E is the input pulse energy (mJ), τ is the pulse width (7 ns), and ω_z is the radius of the focused beam on crystal which is at 5 mm above the focal point and it is denoted as Z. The ω_z can be calculated using following expressions:

$$\omega_Z = \omega_0\sqrt{1+\left(\frac{Z}{Z_R}\right)^2} \tag{15}$$

$$Z_R = \left(\frac{\pi\omega_0^2}{\lambda}\right);\ \omega_0 \geq \frac{2\lambda}{\pi} \tag{16}$$

where λ is the wavelength of laser (532 nm), f is the focal length of convex lens (10 cm) and d is the diameter of laser beam (8 mm). The value of ω_o was estimated to be 10 µm. The Rayleigh length (Z_R) was found to be 590 µm and also condition of $\omega_0 \geq 2\lambda/\pi$ was satisfied. To avoid large peak intensities, the crystal was placed at a distance of 5 mm away from the focus for all the damage threshold studies. The radius of beam spot (ω_z) was estimated and it was found to be ~85.3 µm. The laser power at ω_z (GW/cm^2) and damage dimension (µm) versus successive input energy (mJ) is shown in Fig. 26. The initial damage spot on the AMP4N crystal appeared at 15 mJ and its LDT value was found to be 9.37 GW/cm^2. The higher value of laser damage tolerance is more useful for frequency conversion applications.

4.10. Z-scan studies

The third-order NLO properties of AMP4N crystal were investigated using Z-scan technique [32,36]. In this experiment, the diode laser (25 mW) of wavelength at 532 nm was used as a source and the beam diameter is 5 mm. The polarized Gaussian beam of mode TEM_{00} was focused by a convex lens (focal length is 286.2 mm) to produce the beam waist ω_o = 19.39 µm. The thickness of the sample (L) was

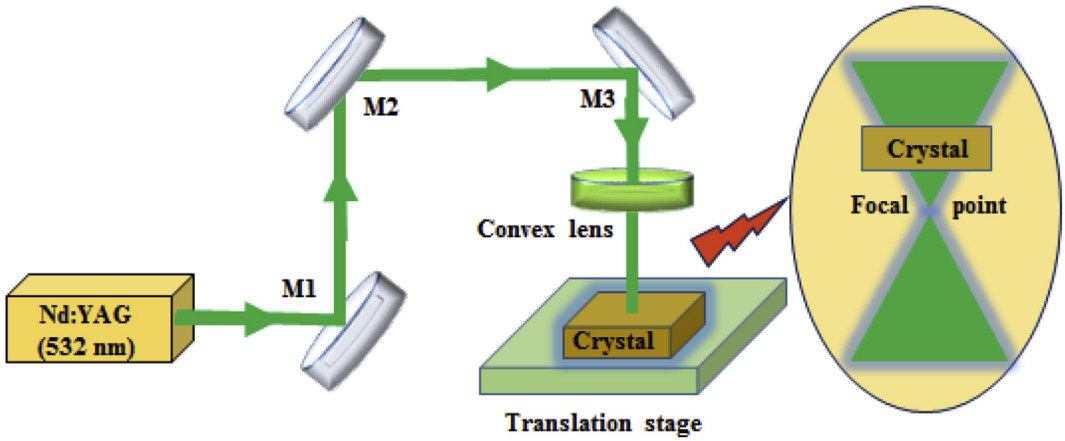

Fig. 24. Schematic diagram of LDT measurement.

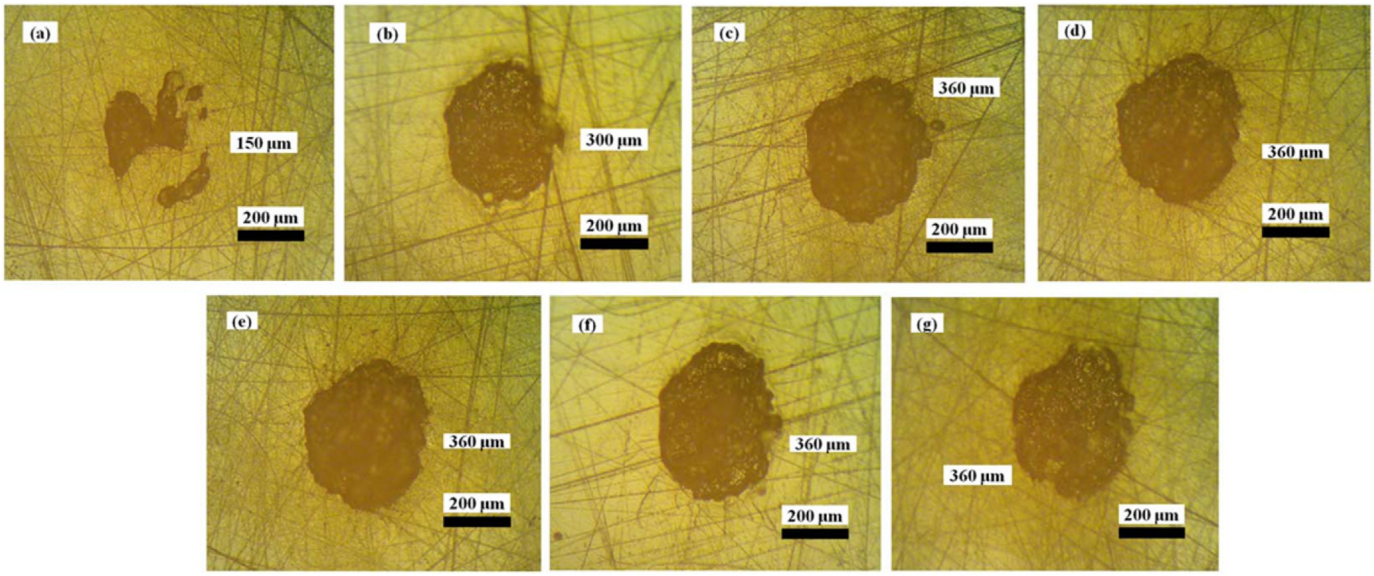

Fig. 25. Laser damage patterns of AMP4N crystal.

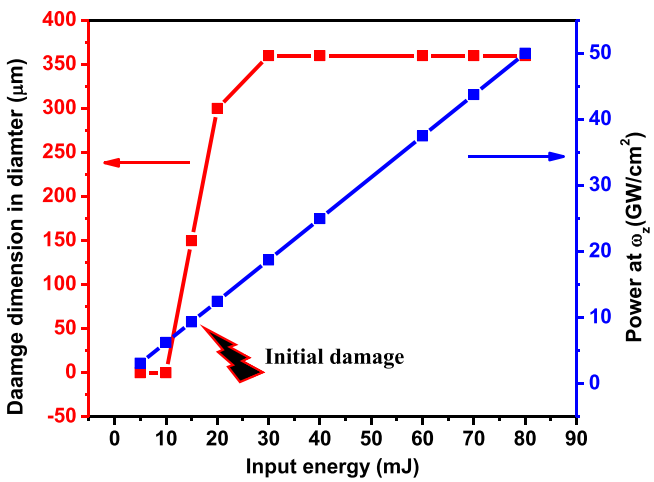

Fig. 26. Laser power at ω_z (GW/cm^2) and damage dimension (µm) and versus successive input energy (mJ).

0.6 mm. The Rayleigh length *(Z_R)* was calculated as 2.22 mm. The thickness of the samples must be less than the Rayleigh length and it was satisfied *($L < Z_R$)*. The sample was fixed on a holder (90°) and it was moved along the negative *(–Z)* to positive *(+Z)* axis, which was parallel to the direction of propagation of the laser beam. The translation of sample holder can be controlled by the computer for the precision of each movement. The corresponding transmitted intensity through the sample was collected by a photodetector and it was measured by the digital power meter. In closed aperture, the received intensity depends on the aperture radius (2 mm) and it was consistent for the entire experimental process. For an open aperture, the intensity was collected directly by the detector to find out nonlinear absorption coefficient *(β)*. Fig. 27 (a) and (b) depict the closed and open aperture Z-scan curves of AMP4N crystal. The intensity of a laser beam directly depends on the refractive index of the materials and its absorption nature. The sample causes an additional focusing or defocusing, depending on the nonlinear refraction values [37]. The minimum transmission at the focus (Z = 0) indicates two or multi photons absorption or reverse saturation of absorption. Materials with strong reverse saturable absorption have been searched for power limiting applications. From the open aperture Z-scan spectrum the non-linear absorption coefficient *(β)* was calculated. However, the closed aperture Z-scan curve with pre-focal valley and post-focal peak indicates a self-focusing process and it is a positive sign for nonlinear refraction [38].

In order to find out the nonlinear refractive index of AMP4N crystal, the difference between the transmittance peak and valley transmission *($\Delta T_{p\text{-}v}$)* was calculated writing the following equation in terms of the axis phase shift at the focus.

$$|\Delta\phi| = \frac{\Delta T_{p-v}}{0.406(1-S)^{0.25}} \tag{17}$$

where $\Delta\varphi$ is the axis phase shift at the focus, S is the linear transmittance aperture and it was calculated using the relation:

$$S = 1 - \exp\left(\frac{-2r_a^2}{\omega_a^2}\right) \tag{18}$$

where r_a is the radius of aperture (2 mm) and ω_a is the beam radius at the aperture (3.3 mm). The nonlinear refractive index *(n_2)* was calculated using the relation:

$$n_2 = \frac{\Delta\varphi}{kI_0L_{eff}}\,(m^2/W) \tag{19}$$

The nonlinear absorption coefficient *(β)* was determined using open aperture. The value of β would be positive for two or multi-photon absorptions and negative for saturable absorption.

$$\beta = \frac{2\sqrt{2}\Delta T}{I_0L_{eff}}\,(m/W) \tag{20}$$

where k is the wave number *($k = 2\pi/\lambda$)*, ΔT is the peak value at the open aperture Z – scan curve and I_0 is the intensity of the laser at the focus (21.16 MW/m^2). The effective thickness *(L_{eff})* of the sample was calculated by using the following expression:

$$L_{eff} = \frac{1-\exp(-\alpha L)}{\alpha} \tag{21}$$

where α is the linear absorption coefficient and L is the thickness of the sample (0.6 mm). The effective thickness *(L_{eff})* was found to be 0.5 mm. The real and imaginary parts of the third order nonlinear optical susceptibility *($\chi^{(3)}$)* were estimated using the following relations [39]:

$$R_e\chi^{(3)}\,(esu) = \frac{10^{-4}\varepsilon_0c^2n_0^2n_2}{\pi}\,(cm^2/W) \tag{22}$$

$$I_m\chi^{(3)}\,(esu) = \frac{10^{-2}\varepsilon_0c^2n_0^2\lambda\beta}{4\pi^2}\,(cm/W) \tag{23}$$

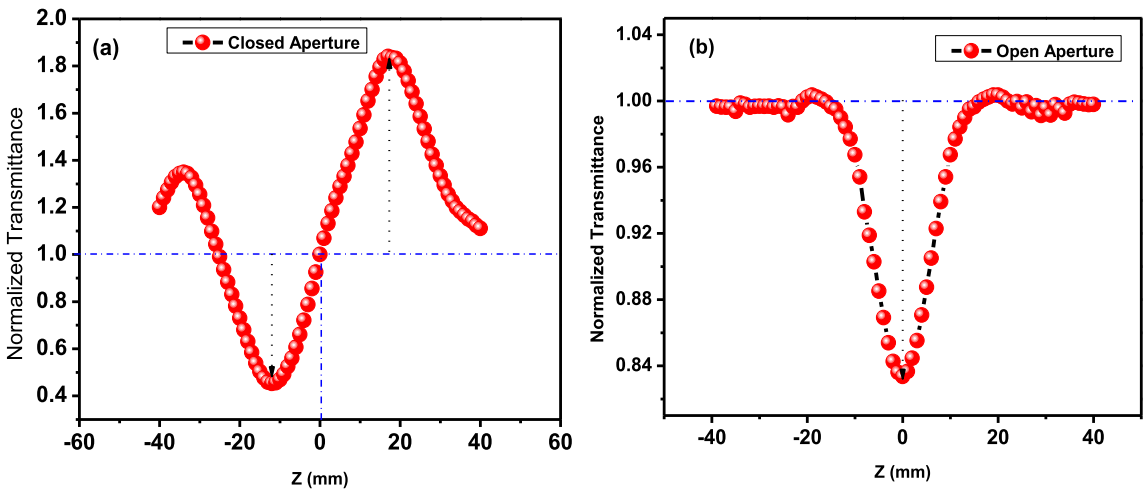

Fig. 27. (a) Closed aperture mode and (b) Open aperture mode Z-scan plot of AMP4N crystal.

where ε_0 is the vacuum permittivity (8.854×10^{-12} F/m), c is the velocity of light in vacuum (3×10^8 m/s), n_0 is the linear refractive index (2.26) of the sample at 532 nm and λ is the wavelength of laser beam. The third order nonlinear optical susceptibility of the grown crystal was calculated using the expression:

$$\chi^{(3)} = \sqrt{(R_e\chi^{(3)})^2 + (I_m\chi^{(3)})^2} \tag{24}$$

The third order nonlinear refractive index (closed-aperture) 'n_2' is 3.25×10^{-11} m^2/W, the nonlinear absorption coefficient (open-aperture) 'β' is 4.45×10^{-5} m/W and the absolute value of third-order nonlinear susceptibility '$\chi^{(3)}$' is 2.48×10^{-8} esu for AMP4N crystal. The experimental parameters and obtained results are given in the S. Table 3. The third-order susceptibility is found to be larger than several other NLO crystals [40–45] as seen in Table 3. The positive sign of the nonlinear refractive index (n_2) indicates the self-focusing nature of the material. This may have an advantage in practical devices, by providing remote sensing and lightning control [46]. Further, the grown crystal is suitable for optical switches if the conditions $W > 1$ and $T < 1$ are satisfied. W and T were evaluated using the following equations [47].

$$W = \frac{n_2 I_0}{\alpha_0 \lambda} \tag{25}$$

$$T = \frac{\beta\lambda}{n_2} \tag{26}$$

where n_2 is nonlinear refractive index, β is nonlinear absorption coefficient, α_0 is the linear absorption coefficient, λ is the wavelength of laser source and I_0 is the irradiance of the laser beam at focus. The figure of merit was calculated to be $W = 2.30$, and $T = 0.72$. The values of W and T are reasonably good for applications in photonics. The suitability of the sample to be used as optical limiting depends on the sign and the magnitude of nonlinear refractive index and absorption coefficient. The positive nonlinear refractive index and reverse saturation absorption suggested that the AMP4N crystal may be useful for optical limiting applications [47]. Hence, AMP4N crystal is suitable to be used as optical switching and optical limiter devices.

Table 3
Comparison of ($\chi^{(3)}$) values of AMP4N with other NLO materials.

Crystal	Third order susceptibility ($\chi^{(3)}$)	References
AMP4N	**2.483×10^{-08} esu**	**Present work**
$LiKB_4O_7$	4.85×10^{-09} esu (c-axis)	[40]
VMST	9.69×10^{-12} esu	[41]
KBBF	9.4×10^{-14} esu	[42]
BBO	5.7×10^{-14} esu	[43]
HEANP	4.22×10^{-14} esu	[44]
KDP	8.34×10^{-14} esu	[45]

5. Conclusions

The optically highly transparent organic NLO single crystals of 2-amino-4,6-dimethylpyrimidine 4-nitrophenol (AMP4N) were successfully grown by slow evaporation solution technique (SEST) using methanol as solvent. The structure of the grown crystal was solved by the direct method using SHELXS software. Theoretically, the intermolecular interactions between the AMP4N molecules were analyzed by the Hirshfeld surfaces analysis. The crystalline planes and their perfection were identified by the Powder XRD measurement. Also, the lattice strain of the grown crystal was calculated and it becomes low, hence confirms the AMP4N crystal has less lattice strain. The morphology of the grown crystal was indexed using WinXMorph software program. The environment of carbon (C) and hydrogen (H) in the present system was analyzed by the NMR spectroscopy. The presence of functional groups and their different vibrations were confirmed by FTIR spectral analysis. UV–Vis NIR spectrum shows that the crystal becomes transparent in the entire Vis-IR region and the cut-off wavelength was found to be 405 nm. The grown crystal has good optical transparency and hence it is suitable for NLO applications upto 405 nm. The optical band gap was calculated using Tauc's plot relation and it is found to be 3.20 eV. TG-DTA studies indicated that the AMP4N crystal is thermally stable upto 120 °C. There was no phase transition and decomposition below that temperature and hence it may operate for practical applications with temperature upto 120 °C. The mechanical properties confirmed that the material belongs to soft material category. The results of etching studies revealed the growth mechanism of AMP4N crystal to be layer pattern with minimum dislocations. It may be useful for reducing distorted generation of light. The higher value of surface laser damage threshold of AMP4N suggests that these crystals may have a favourable application in laser frequency conversion. The AMP4N crystal was stable up to peak intensity of 9.37 GW/cm^2. The Z-scan experimental results confirmed the large value of nonlinear optical absorption coefficient (β) and nonlinear optical refractive index (n_2). Thus, all the findings of the various studies suggested that AMP4N crystal may be a suitable material for the fabrication of third harmonic generation up to 405 nm, optical switching and optical limiter devices.

Acknowledgements

This work was supported by the BRNS project (Ref. 34/14/06/2016-BRNS/34032), Government of India. The authors thank SAIF, IIT-Madras for single crystal XRD analysis and also thank the Central facility, Sastra University, Thanjavur for the NMR measurement.

Appendix A. Supplementary data

Supplementary data related to this article can be found at https://doi.org/10.1016/j.optmat.2018.07.039.

References

[1] C.C. Evans, M.B. Beucher, R. Masse, J.F. Nicoud, Chem. Mater. 10 (1998) 847–854.
[2] J. Badan, R. Hierle, A. Perigaud, J. Zuss (Eds.), Non-linear Optical Properties of Organic Molecules and Polymeric Materials, American Chemical Symposium Series 233, American Chemical Society, Washington. DC, 1993.
[3] G.A. Jeffrey, W. Saenger, Hydrogen Bonding in Biological Structures, Springer-Verlag, Berlin, 1991.
[4] P. Srinivasan, Y. Vidyalakshmi, R. Gopalakrishnan, Cryst. Growth Des. 8 (2008) 2329–2334.
[5] M. Mahadevan, K. Ramachandran, P. Anandan, M. Arivanandhan, G. Bhagavannarayana, Y. Hayakawa, Spectrochim. Acta, Part a 133 (2014) 396–402.
[6] T. Kolev, R.W. Seidel, B.B. Koleva, et al., Struct. Chem. 19 (2008) 101–107.
[7] A.J. Barnes, J. Mol. Struct. 704 (2004) 3–9.
[8] M. Hemamalini, W.S. Loh, C.K. Quah, H.K. Fun, Chem Cent J. Journal 8 (2014) 31.
[9] V. Krishnakumar, S. Kalyaranaman, M. Piasecki, I.V. Kityk, P. Bragiel, J. Raman Spectrosc. 39 (2008) 1450–1454.
[10] G.M. Sheldrick, Acta Crystallogr. A64 (2008) 112–122.
[11] C.F. Macrae, I.J. Bruno, J.A. Chisholm, P.R. Edgington, P. McCabe, E. Pidcock, L. Rodriguez-Monge, R. Taylor, J.V.D. Streek, P.A. Wood, J. Appl. Crystallogr. 41 (2008) 466–470.
[12] L.J. Farrugia, J. Appl. Crystallogr. B 30 (1997) 565.
[13] P. Devi, P. Thomas Muthiah, Acta Crystallogr. E63 (2007) o4822–o4823.
[14] S. Ebenezer, P.T. Muthiah, R.J. Butcher, Cryst. Growth Des. 11 (2011) 3579–3592.
[15] S. Muralidharan, P. Nagapandiselvi, T. Srinivasan, Y. Vidyalakshmi, D. Velmurugan, R. Gopalakrishnan, Asian J. Chem. 25 (2013) 10107–10112.
[16] M.A. Spackman, D. Jayatilaka, CrystEngComm 11 (2009) 19–32.
[17] S.K. Wolff, D.J. Grimwood, J.J. McKinnon, M.J. Turner, D. Jayatilaka, M.A. Spackman, Crystal Explorer (Version 3.0), University of Western Australia, 2010.
[18] V.D. Mote, Y. Purushotham, B.N. Dole, J Theor Appl Phys. 6 (2012) 6.
[19] N. Kanagathara, M.K. Marchewka, M. Drozd, N.G. Renganathan, S. Gunasekaran, G. Anbalagan, J. Mol. Struct. 1049 (2013) 345–354.
[20] D.N. Sathyanarayana, Vibrational Spectroscopy, Theory and Applications, New Age International (P) Limited Publishers, New Delhi, 1996.
[21] L.N. Wang, X.Q. Wang, G.H. Zhang, X.T. Liu, Z.H. Sun, G.H. Sun, L. Wang, W.T. Yu, D. Yu, J. Cryst. Growth 327 (2011) 133–139.
[22] N. Sundaraganesan, B. Anand, B. Dominic Joshua, Spectrochim. Acta 65 (2006) 1053–1062.
[23] M. Jose, B. Sridhar, G. Bhagavannarayana, K. Suganthi, R. Uthrakumar, C. Justin Raj, D. Tamilvendhan, S. Jerome Das, J. Cryst. Growth 312 (2010) 793–799.
[24] M.I. Khan, A. Ahmad, M.F. Ullah, J. Photochem. Photobiol., B 103 (2011) 42–49.
[25] M.K. Marchewka, A. Pietraszko, H. Feki, Y. Abid, Vib. Spectrosc. 56 (2011) 255–264.
[26] A.H. Reshak, D. Stys, S. Auluck, I.V. Kityk, Phys. Chem. Chem. Phys. 12 (2010) 2975–2980.
[27] A.H. Reshak, D. Stys, S. Auluck, I.V. Kityk, J. Phys. Chem. B 114 (2010) 1815–1821.
[28] J. Tauc, R. Grigorovici, A. Vancu, Phys. Status Solidi B15 (1996) 627–637.
[29] N. Chopra, A. Mansingh, G.K. Chadha, J. Non-cryst. Solids 126 (1990) 194–201.
[30] P. Karuppasamy, V. Sivasubramani, M. Senthil Pandian, P. Ramasamy, RSC Adv. 6 (2016) 109105–109123.
[31] G. Om Reddy, K.S. Ravikumar, Thermochim. Acta 198 (1992) 147–165.
[32] P. Karuppasamy, M. Senthil Pandian, P. Ramasamy, Sunil Verma, Opt. Mater. 79 (2018) 152–171.
[33] K. Sangwal, Mater. Chem. Phys. 63 (2000) 145–152.
[34] E. Meyer, Z. Ver, Dtsch. IngenieurBlatt 52 (1908) 645–654.
[35] H. Yoshida, H. Fujita, M. Nakatsuka, M. Yoshimura, T. Sasaki, T. Kamimura, K. Yoshida, Jpn. J. Appl. Phys. 45 (2006) 766–769.
[36] M. Sheik-Bahae, A.A. Said, T. Wei, D.J. Hagan, E.W. Van Stryland, IEEE J. Quant. Electron. 26 (1990) 760–769.
[37] M. Sheik-Bahae, A.A. Said, E.W. Van Stryland, Opt. Lett. 14 (1989) 955–957.
[38] I. Bhattacharyya, S. Priyadarshi, D. Goswami, Chem. Phys. Lett. 469 (2009) 104–109.
[39] P. Karuppasamy, M. Senthil Pandian, P. Ramasamy, J. Cryst. Growth 473 (2017) 39–54.
[40] M. Sukumar, R. Ramesh Babu, K. Ramamurthi, Appl. Phys. B 121 (2015) 369–373.
[41] M.K. Kumar, S. Sudhahar, P. Pandi, G. Bhagavannarayana, R.M. Kumar, Opt. Mater. 36 (2014) 988–995.
[42] F.Q. Li, N. Zong, F.F. Zhang, J. Yang, F. Yang, Q.J. Peng, D.F. Cui, J.Y. Zhang, X.Y. Wang, C.T. Chen, Z.Y. Xu, Appl. Phys. B 108 (2012) 301–305.
[43] M. Yin, H.P. Li, S.H. Tang, W. Ji, Appl. Phys. B 70 (2000) 587–591.
[44] N. Sudharsana, V. Krishnakumar, R. Nagalakshmi, J. Cryst. Growth 398 (2014) 45–57.
[45] D. Wang, T. Li, S. Wang, J. Wang, Z. Wang, X. Xu, F. Zhang, RSC Adv. 6 (2016) 14490–14495.
[46] R.W. Boyd, S.G. Lukishova, Y.R. Shen, Self-focusing: past and present: fundamentals and prospects, Top. Appl. Phys. 114 (2009).
[47] H. Fan, Q. Ren, X. Wang, T. Li, J. Sun, G. Zhang, D. Xu, G. Yu, Z. Sun, Nat. Sci. 1 (2009) 136–141.